Electronic Supplementary Material (ESI) for Journal of Materials Chemistry A.

Supporting Information

An Ultrathin and Highly Porous Silica Nanochannel Membrane: Toward Highly Efficient Salinity Energy Conversion

*Fei Yan, Lina Yao, Kexin Chen, Qian Yang, and Bin Su**
Institute of Analytical Chemistry, Department of Chemistry, Zhejiang University, Hangzhou 310058, China

Table of Contents

S1. Preparation of SIM

S2. Characterizations of SIM

S2.1. Electrochemical characterizations

S2.2. TEM, SEM and metallographic characterizations

S3. Estimation of surface charge density of SIM

S4. Salinity-gradient-driven ICR in SIM

S5. Numerical simulation

S5.1. Governing equations

S5.2. Simulation model

S6. Equivalent circuit for energy conversion

S7. Energy conversion simulation

S8. Comparison of the energy conversion performance of SIM with other membranes

S1. Preparation of SIM

As illustrated in **Scheme S1**, SIM was firstly grown on the ITO glass using the Stöber-solution growth approach.[S1] Typically, the ITO glasses were immersed in the precursor solution containing 70 mL water, 30 mL ethanol, 0.16 g CTAB, 10 μL concentrated ammonia aqueous solution and 80 μL TEOS. By a simple solution spontaneous growth for 24 h under the quiescent condition at 60 °C, SIM with CTAB micelles confined in silica nanochannels was formed on the ITO surface, designated as micelles@SIM/ITO. After dissolving micelles by immersing in 0.1 M HCl/ethanol solution under stirring for 20 min, SIM/ITO was obtained.

SIM/SiN was prepared using the PMMA-assisted transfer approach as previously reported.[S2] Briefly, PMMA solution (3.5% wt in anisole) was spin-coated on the top surface of SIM/ITO at 2000 rpm for 30 s. After solvent evaporation at room temperature for 1 h and heating at 115 °C for 15 min, the obtained PMMA protected SIM/ITO was treated with 2 M HCl to etch the ITO layer and lift off the free-standing PMMA/SIM. Subsequently, a piece of commercial SiN window with a single 6-μm-diameter pore was used as the substrate to fish out the free-standing PMMA/SIM. Finally, the top PMMA layer was dissolved by acetone to obtain perforated nanochannels.

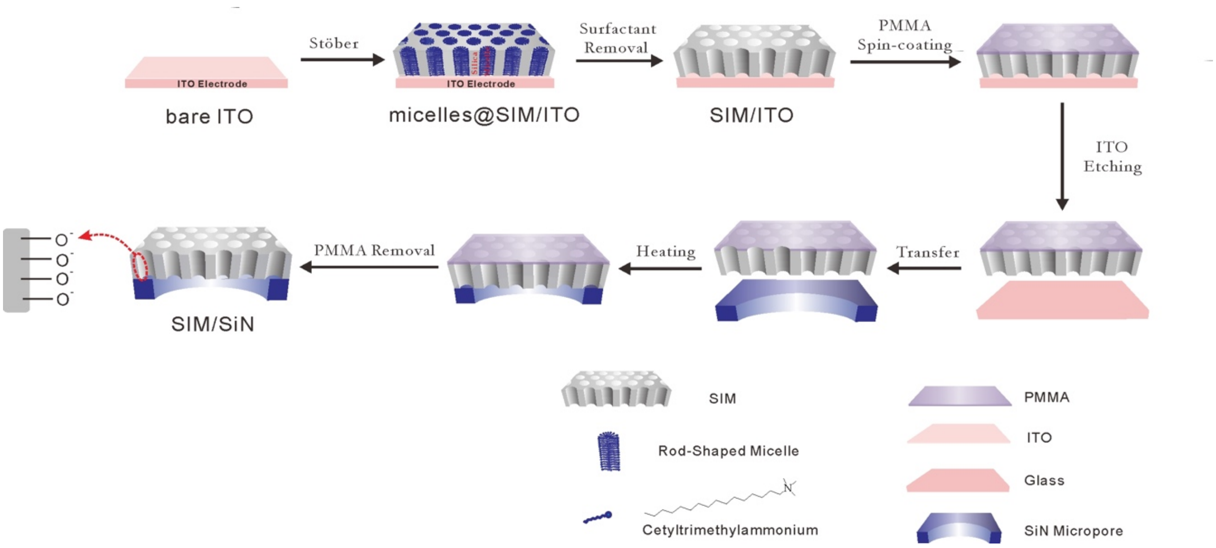

Scheme S1. Schematic illustration of the preparation of SIM/SiN

S2. Characterizations of SIM

S2.1. Electrochemical characterizations

SIM/ITO was characterized by CV. As shown in **Figure S1**, at the micelles@SIM/ITO electrode, only a capacitive current was displayed for charged probes, ($Ru(NH_3)_6^{3+}$ and $Fe(CN)_6^{3-}$, indicating the SIM was compact without cracks. Note that after removal of micelles, the SIM/ITO electrode showed an apparent ion selectivity, repelling negatively charged $Fe(CN)_6^{3-}$ and attracting positively charged $Ru(NH_3)_6^{3+}$. The ion selectivity principally arises from ultrasmall size of silica nanochannels (2~3 in diameter) and their negatively charged wall (the isoelectric point of silanol group is 2~3).[S3] In addition, the SIM/ITO electrode presents a current magnitude comparable to that of a bare ITO electrode, indicating the high molecular permeability of SIM.

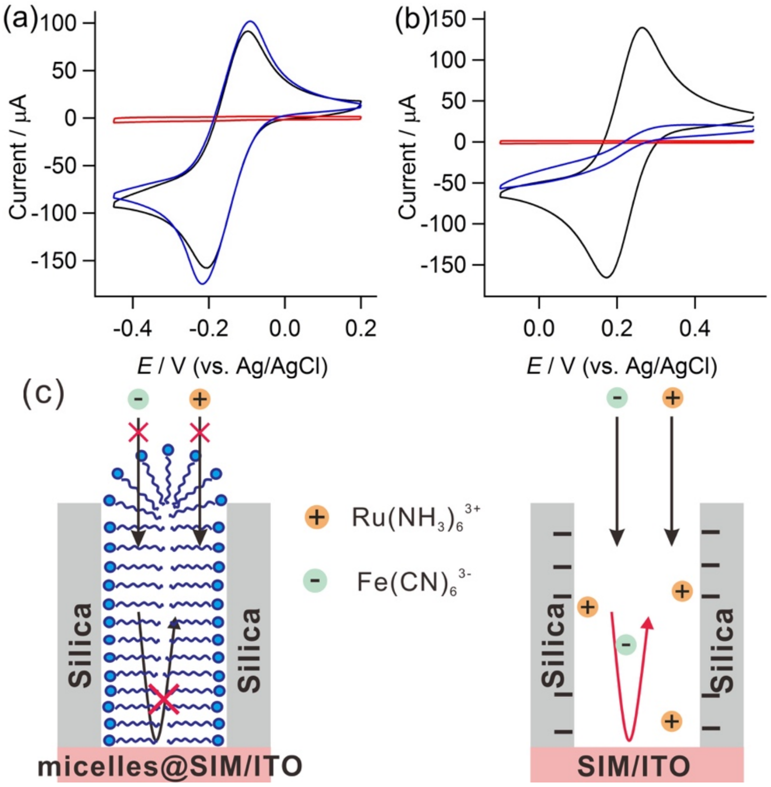

Figure S1. (a, b) CVs of 0.5 mM $Ru(NH_3)_6^{3+}$ (a) and $Fe(CN)_6^{3-}$ (b) at a bare ITO (black), micelles@SIM/ITO (red) and SIM/ITO (blue) electrodes in 0.05 M KHP solutions. The scan rate was 50 mV/s and the electrode area was 2.5 cm^2. (c) Schematic illustration of mass transport of redox probes at the micelles@SIM/ITO and SIM/ITO electrodes.

S2.2. TEM, SEM and metallographic characterizations

Figure S2a-d show the metallographs (a, b) and top-view SEM images (c, d) of a bare SiN (a, c) and SIM/SiN (b, d), respectively. As seen in **Figures S2a** and **S2c**, a single pore could be found in the center of SiN window. After SIM was transferred to its top surface, the brightness of 6-μm-diameter pore turned a bit dark but still visible, proving that the SIM is ultrathin. The thickness of SIM was ca. 90 nm, as revealed by the cross-section SEM image (see **Figure S2e**). **Figure S2f** displays the top-view TEM image, in which well-defined nanopores are clearly identified as bright spots, with a uniform size (2−3 nm in diameter) and a high pore density (4.0 × 10^{12} cm^{-2}, corresponding to a porosity of 16.7%).

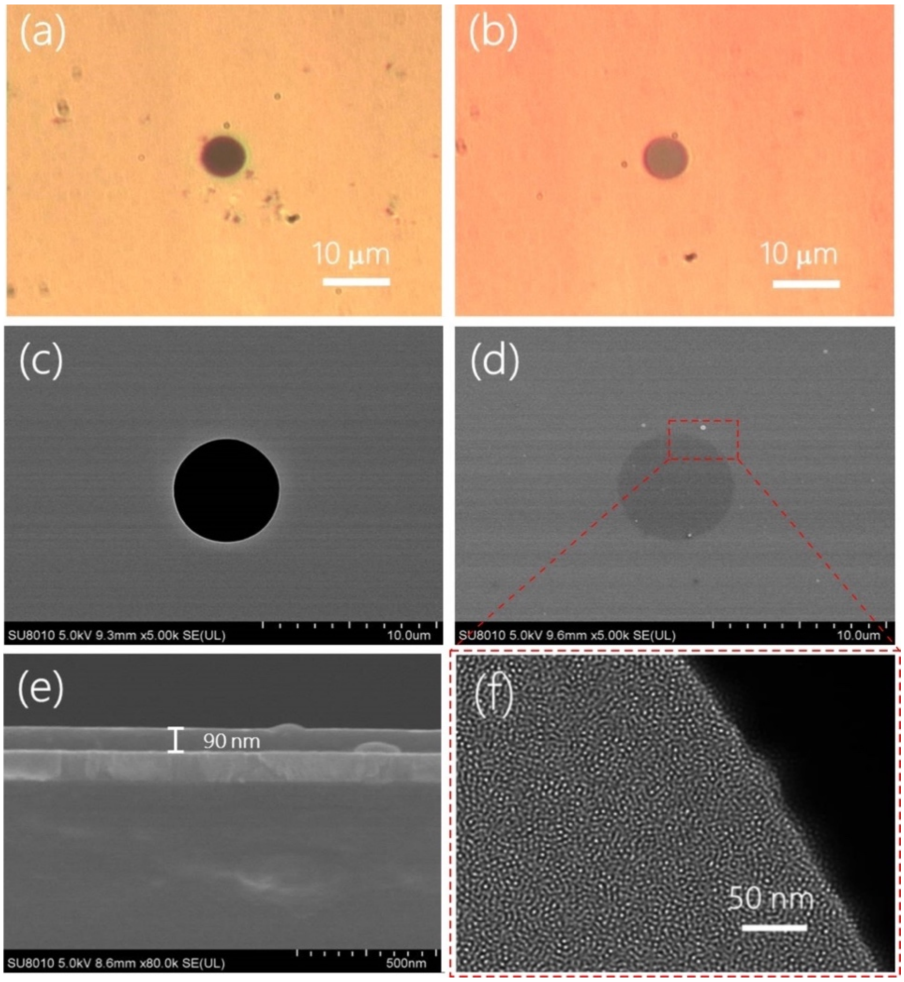

Figure S2. Metallographs (a, b) and top-view SEM (c, d) images of a bare SiN window with a single 6-μm-diameter pore before (a, c) and after (b, d) supporting SIM. (e) Cross-sectional SEM image showing the SIM layer on the ITO electrode with a thickness of ca. 90 nm. (f) High-magnification top-view TEM image of SIM supported by SiN window.

S3. Estimation of surface charge density of SIM

The nanochannel diameter of SIM is 2~3 nm and comparable to the Debye length. When the nanochannels of SIM are filled with electrolyte solution, SIM shows ion selectivity, repelling the access of anions and allowing that of cations. Therefore, at the relatively low concentration of electrolyte, ion conductance of SIM (G_{SIM}) is governed by the surface charge of nanchannels instead of the bulk electrolyte concentration. Based on this point, G_{SIM} was estimated from the ionic conductance measurements, which was employed in turn to calculate the surface charge density (σ). SIM/SiN and bare SiN was mounted to the cell shown in **Figure 1b**, where two compartments were filled with the same solution containing KCl.

Considering SIM and SiN pore are in series, G_{SIM} was given by the following equation,

$$G_{\mathrm{SIM}} = \left[\frac{1}{G_{\mathrm{SIM/SiN}}} - \frac{1}{G_{\mathrm{SiN}}} \right]^{-1} \qquad \text{(S1)}$$

where $G_{\mathrm{SIM/SiN}}$ and G_{SiN} represent the ionic conductance of SIM/SiN and bare SiN. **Figure S3a-i** shows *I*–*V* curves obtained for the concentrations of KCl varied from 10^{-4} M to 1 M. They are almost linear for every concentration with a large conductance. This is because the negatively charged SIM under the testing condition possesses a symmetric channel structure and a high pore density. Further plotting $G_{\mathrm{SIM/SiN}}$ versus KCl concentration yielded a curve with an inflexion and a saturation plateau in the low concentration range. In contrast, G_{SiN} is always proportional to the KCl concentration under the same condition (see **Figure S4**), showing typical characteristic of bulk solution behavior. It also indicates that the SiN pore functions only as the support and does not influence the ion transport selectivity through SIM.

With above data and equation (S1), G_{SIM} was extracted and shown in **Figure S3k**. Apparently, G_{SIM} exhibits an inflexion and reaches to a saturation plateau in the low concentration range, indicative of a surface-charge-governed ionic transport inside nanochannels of SIM under this situation.

For nanochannels with small aspect ratio, the overall conductance is given by,[S4]

$$G_{\mathrm{SIM}} = \kappa_{\mathrm{b}} \left[\frac{L}{\pi a^{2}} \cdot \frac{1}{1 + \frac{2\kappa_{\mathrm{s}}}{\kappa_{\mathrm{b}} a}} + \frac{2}{2\alpha a + \beta \frac{\kappa_{\mathrm{s}}}{\kappa_{\mathrm{b}}}} \right]^{-1} \tag{S2}$$

where κ_{b} and κ_{s} are bulk and surface conductivities, respectively. L and a are the length and radius of nanochannel, respectively. α is a geometrical pre-factor that depends on the model used and β is a numerical constant (here $\alpha = \beta = 2$). Moreover, $\kappa_{\mathrm{s}}/\kappa_{\mathrm{b}}$ is approximately equal to $\sigma/2Fc_{\mathrm{b}}$ (σ is the surface charge density, F is the Faraday constant, and c_{b} is the electrolyte concentration, respectively). By fitting the experimental data to equation (S2), as shown in **Figure S3k**, σ was estimated to be ca. −0.015 C/m^2.

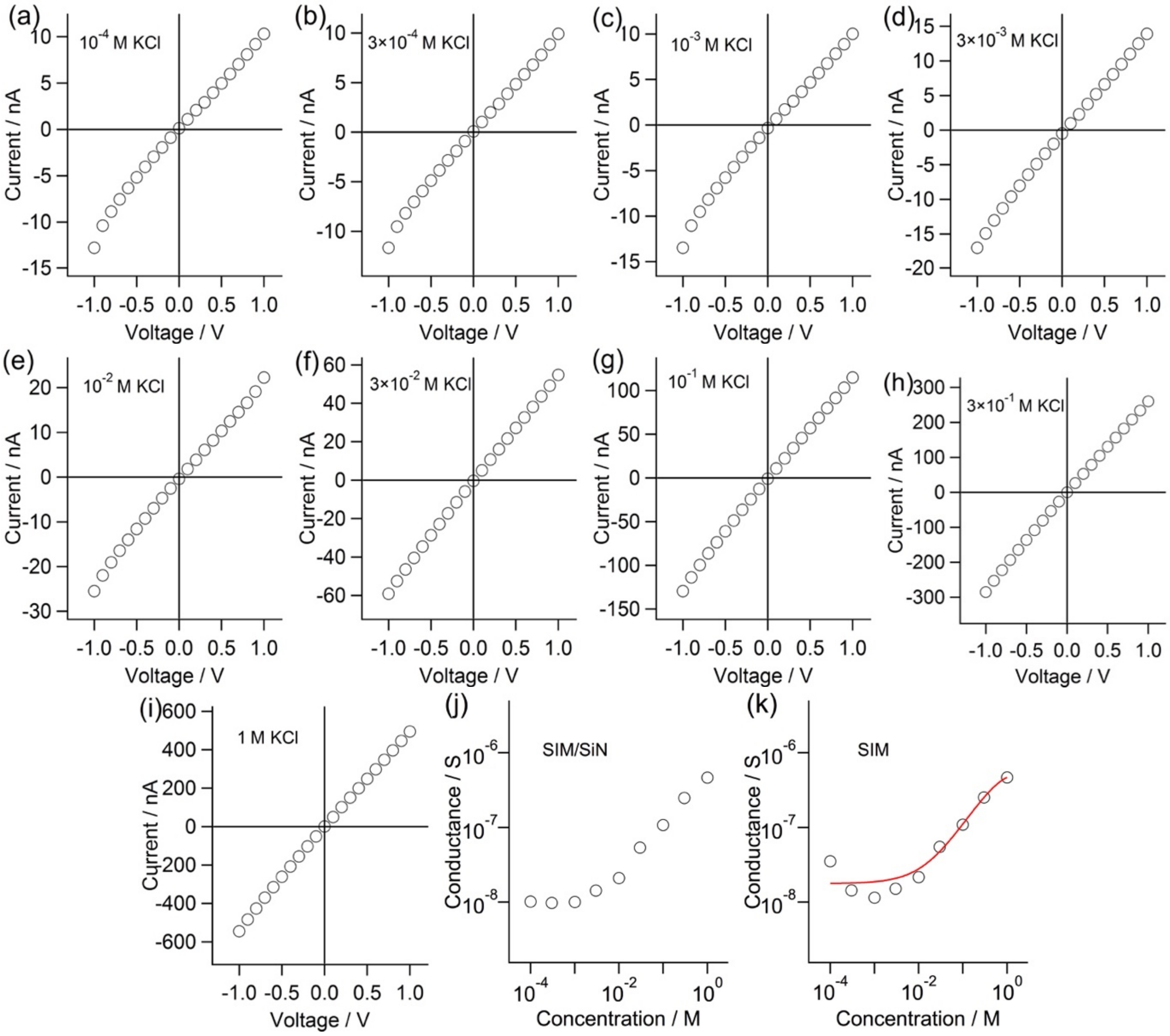

Figure S3. (a-i) Measured *I*−*V* curves of SIN/SiN under various concentrations of KCl from 10^{-4} M to 1 M. (j, k) The dependence of measured ionic conductance of SIM/SiN (j) and SIM (k) on the concentration of KCl.

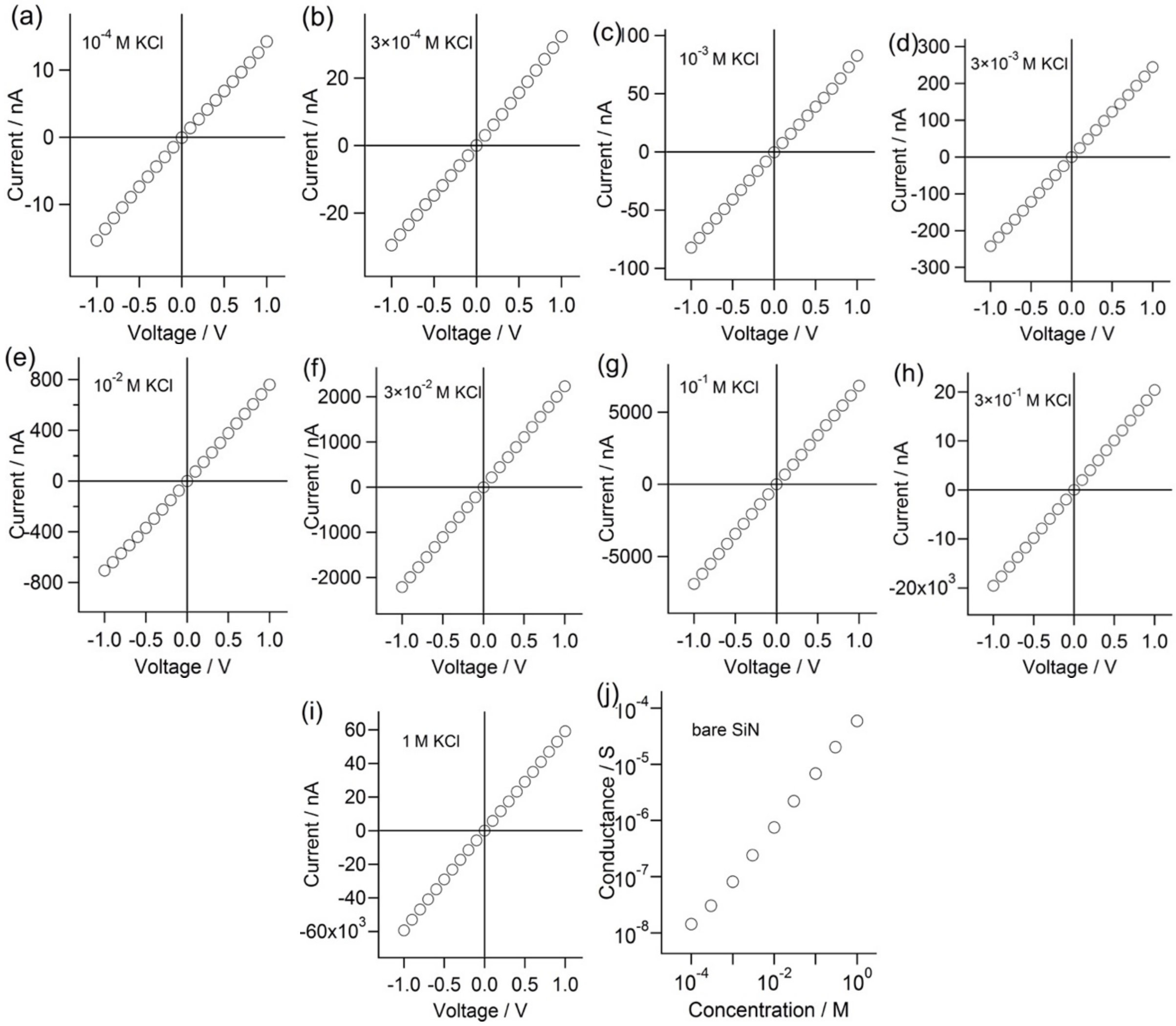

Figure S4. (a-i) Measured *I*−*V* curves of bare SiN under various concentrations of KCl from 10^{-4} M to 1 M. (j) The dependence of measured conductance on the concentration of KCl. The transmembrane ionic conductance of the bare SiN (6 μm in diameter) is linearly dependent on the KCl concentration, indicating a bulk-characteristic ion transport.

S4. Salinity-gradient-driven ICR by SIM

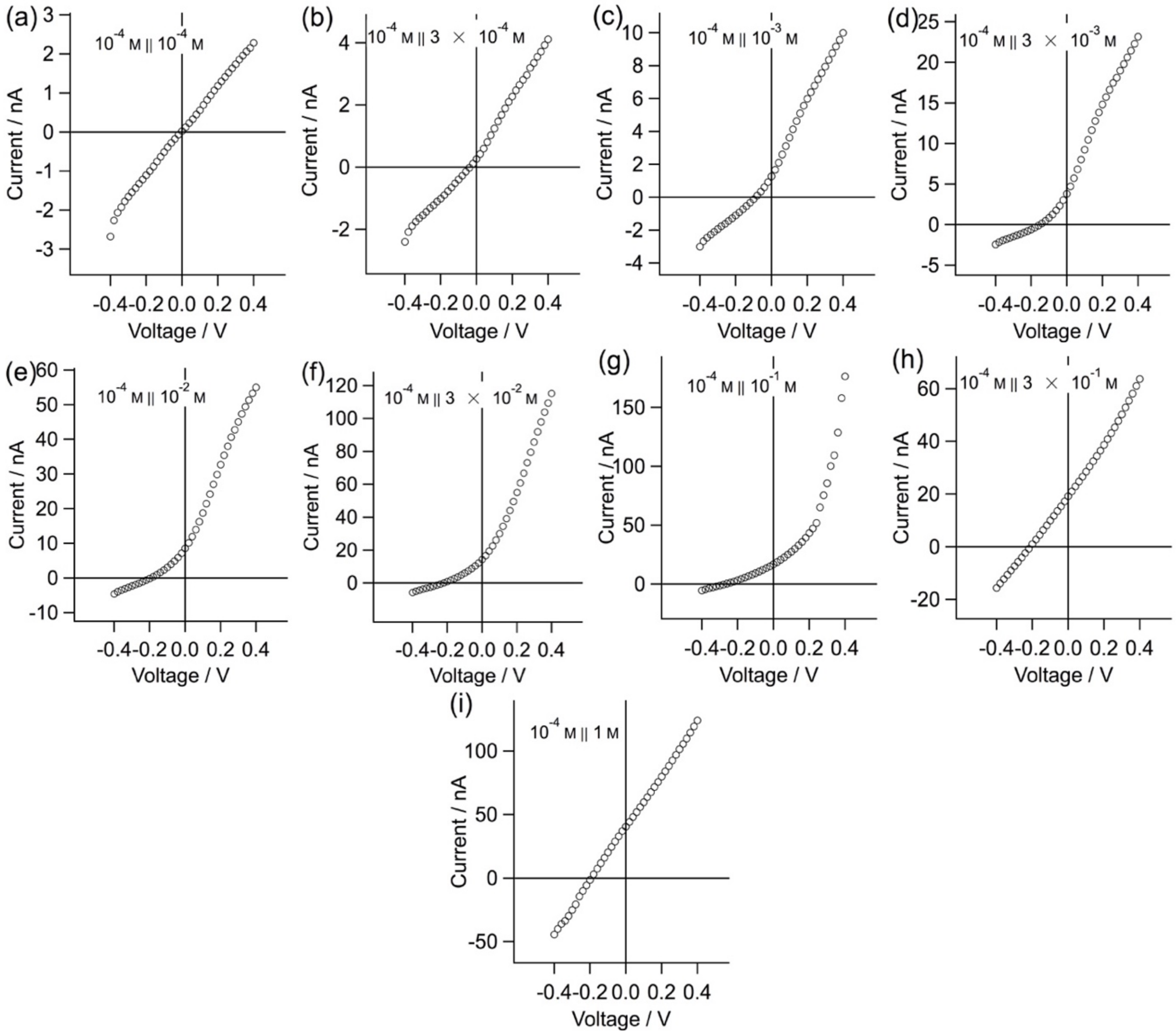

Figure S5. (a-i) Measured *I*−*V* curves of SIM/SiN under a series of c_H/c_L with c_L fixed at 10^{-4} M and c_H varied from 10^{-4} M to 1 M.

S5. Numerical simulation

S5.1. Governing equations

A concentration-gradient-driven ion flow through the nanochannels of cation-selective SIM generates net electrical current, which could convert Gibbs free energy in the form of a salinity gradient into electricity. Therefore, electrical current generated is considerably related with asymmetric transport of cations and anions. In order to understand the ionic transport process through the nanochannel of SIM under various concentration gradients, numerical simulation based on the coupled Poisson and Nernst−Planck (PNP) equations was performed using finite element software COMSOL Multiphysics (version 5.2). Two modules, "electrostatics" and "transport of diluted species", were used,

$$\nabla^2\phi = -\frac{\rho}{\varepsilon} = -\frac{F}{\varepsilon}\sum_i z_i c_i \tag{S3}$$

$$\mathbf{j}_i = -D_i\left(\nabla c_i + \frac{z_i F c_i}{RT}\nabla\phi\right) \tag{S4}$$

$$\nabla\cdot\mathbf{j}_i = 0 \tag{S5}$$

where ϕ [V] and ρ [C/m^3] are the electric potential and space charge density. $\mathbf{j}_i$ [mol/(m^2 s)], z_i [-], c_i [M], D_i [m^2/s] are the ionic flux, charge number, concentration, diffusion coefficient of ion i, respectively (i = + for K$^+$, and i = − for Cl$^-$). ε [F/m], F [C/mol], R [J/K/mol], T [K] are permittivity, Faraday constant, ideal gas constant, and absolute temperature, respectively. Diffusion coefficients of K$^+$ and Cl$^-$ are 1.96×10^{-9} m^2/s and 2.0×10^{-9} m^2/s, termed as D_+ and D_-, respectively.

Poisson equation (S3) describes the relationship between ϕ and c_i. Nernst−Planck equation (S4) describes the diffusive and migration fluxes of ions. Under the steady-state condition, Equation (S5) denotes that the ionic transport inside nanochannels is time-independent. By integrating the ionic flux density over the cross section of nanochannel, the total diffusion current was obtained:

$$I = -2\pi F \int (J_+ - J_-) r\mathbf{n}\mathrm{d}r \tag{S6}$$

where r refers to the radius of nanochannel and **n** is the unit outer normal vector.

The power of porous membrane could be calculated by

$$P_{\max} = \frac{1}{4} I \cdot E_{\mathrm{diff}} \cdot N \tag{S7}$$

where N refers to the pore number of SIM supported on SiN window.

S5.2. Simulation model

A single-pore model with 2D axial symmetry has already been widely used to simulate the ion transport behavior in ion-selective nanopores and nanochannel.[S5-S10] Here, we used the 2D axial symmetric model (see **Figure S6**) to simulate energy conversion in SIM. As shown in **Figure S6**, the model consists of a single nanochannel (radius R_n = 1.15 nm and length L_n = 90 nm) connecting two identical reservoirs of radius R_r and length L_r ($R_r = L_r$ = 1000 nm) on each side. The wall of nanochannel are negatively charged and the surface charge density, σ, is set to −0.015 C/m^2 according to the experimental results (Supporting information S3). The top and the bottom reservoirs are filled with KCl solutions (c_H/c_L with c_L fixed at 10^{-4} M and c_H varied from 10^{-4} M to 1 M). **Table S1** summarizes the boundary conditions for this 2D axisymmetric single-pore model.

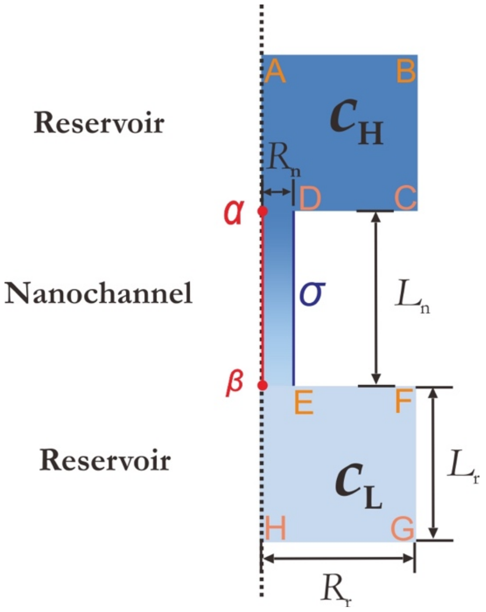

Figure S6. Schematic illustration of the 2D axisymmetric model.

Table S1. Boundary conditions for 2D axisymmetric model

Boundary	Poisson equation	Nernst—Planck equation
AB	applied voltage, $\phi = V$	bulk concentration $c_+ = c_- = c_\mathrm{H}$
GH	grounded, $\phi = 0$	bulk concentration $c_+ = c_- = c_\mathrm{L}$
BC, FG	insulation, $-\mathbf{n}\cdot\nabla\phi = 0$	zero normal ionic flux $\mathbf{n}\cdot\boldsymbol{J}_i = 0$
CD, EF	uncharged, $-\mathbf{n}\cdot\nabla\phi = 0$	ion-impenetrable $\mathbf{n}\cdot\boldsymbol{J}_i = 0$
DE	constant surface charge density $-\varepsilon\mathbf{n}\cdot\nabla\phi = \sigma$	ion-impenetrable $\mathbf{n}\cdot\boldsymbol{J}_i = 0$

n: the unit outer normal vector.

S6. Equivalent circuit for energy conversion

Figure S7 shows the equivalent circuit of experimental test system (a) and energy conversion system (b). As seen in **Figure S7a**, V_{app}, E_{redox}, E_{diff} and R_{channel} represent the potential applied by a source meter, the redox potential difference between two Ag/AgCl electrodes due to the asymmetric redox reaction, diffusion potential of SIM nanofluidic power source, and the internal resistance of SIM/SiN, respectively. E_{diff} is contributed by SIM nanofluidic power sourece and can be experimentally extracted by subtracting E_{redox} from V_{app}, according to the equivalent circuit of experimental setup shown in **Figure S7a**. V_{app} can be obtained from the *V*-intercept of *I-V* curves of SIM/SiN under various concentration gradients. The measured E_{redox} by using salt bridge was similar with the theoretical values calculated by the Nernst equation,

$$E_{\mathrm{redox}} = \frac{RT}{zF} \ln \frac{\gamma_{c_{\mathrm{H}}} c_{\mathrm{H}}}{\gamma_{c_{\mathrm{K}}} c_{\mathrm{L}}} \tag{S8}$$

where $\gamma_{c_{\mathrm{H}}}$ and $\gamma_{c_{\mathrm{L}}}$ are the ionic activity coefficients in two solutions. If V_{app} and E_{redox} were replacing with external elecrtrical load (R_{load}), as shown in **Figure S7b**, SIM under a salinity gradient can be regarded as nanofluidic power source.

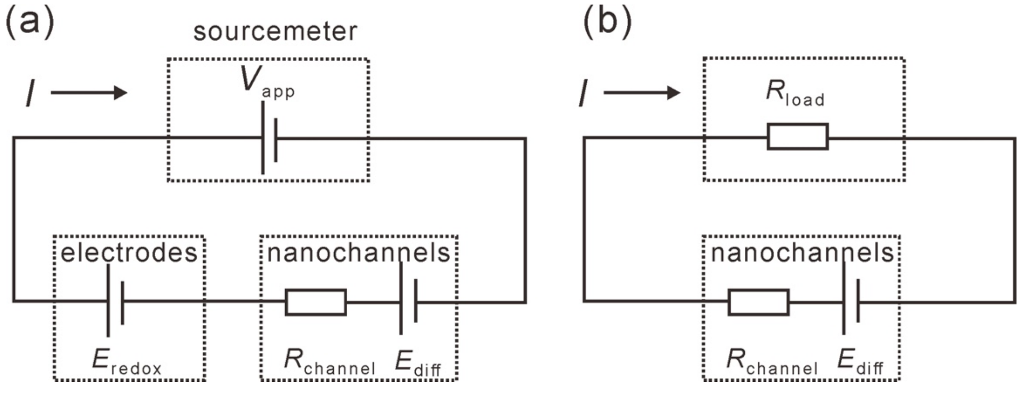

Figure S7. Equivalent circuits of ion transport through SIM under a concentration gradient. (a) Experimental setup system, (b) salinity-gradient-driven power harvesting system based on SIM.

Table S2 summarizes V_{app}, E_{redox} and E_{diff} at various concentration gradients.

Table S2. The measured V_{app}, E_{redox} and E_{diff}

Concentration gradient (M/M)	$10^{-4}/3 \times 10^{-4}$	$10^{-4}/10^{-3}$	$10^{-4}/3 \times 10^{-3}$	$10^{-4}/10^{-2}$	$10^{-4}/3 \times 10^{-2}$	$10^{-4}/10^{-1}$	$10^{-4}/3 \times 10^{-1}$
V_{app} (mV)	36.33	88.68	151.38	193.66	224.97	270.03	211.84
E_{redox} (mV)	28.86	63.61	89.70	125.69	153.90	182.23	198.66
E_{diff} (mV)	7.48	25.07	61.68	67.97	71.07	87.81	13.18

S7. Energy conversion simulation

Figure S8 shows simulated results of E_{diff} and I_{sc} (a), and P_{max} (b) under various $c_{\mathrm{H}}/c_{\mathrm{L}}$. As seen from **Figure S8a**, I_{sc} increases with increasing $c_{\mathrm{H}}/c_{\mathrm{L}}$. The variation of E_{diff} with $c_{\mathrm{H}}/c_{\mathrm{L}}$ shows a maximum at a medium value of $c_{\mathrm{H}}/c_{\mathrm{L}}$. This is because the electrostatic screening effect of EDL inside nanochannels becomes weak at a high value of $c_{\mathrm{H}}/c_{\mathrm{L}}$, leading to a weak permselectivity. **Figure S8b** shows the variation of P_{max} with $c_{\mathrm{H}}/c_{\mathrm{L}}$. P_{max} increases with the increase of $c_{\mathrm{H}}/c_{\mathrm{L}}$, displaying the same variation ratio with the experimental results (see **Figure 3b**). When $c_{\mathrm{H}}/c_{\mathrm{L}}$ is 3000, the increase becomes slower, showing the slightly weaker effect of surface charge.

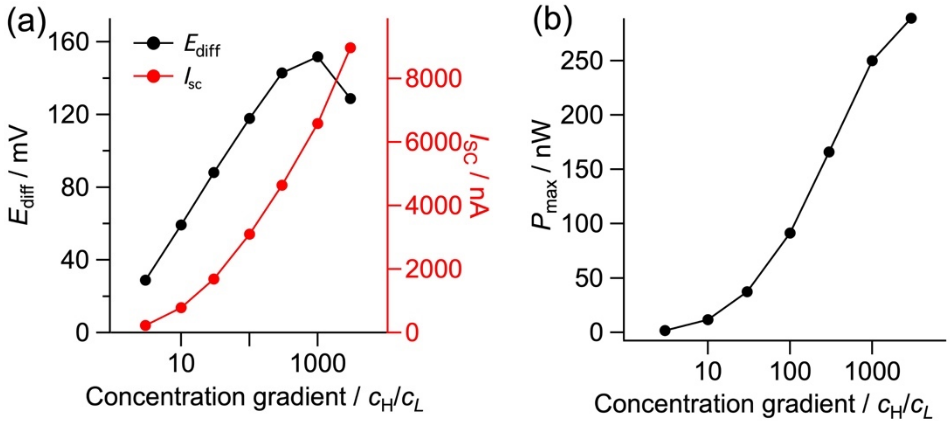

Figure S8. Numerical simulation of energy conversion parameters under various $c_{\mathrm{H}}/c_{\mathrm{L}}$.

S8. Comparison of the energy conversion performance of SIM with other membranes

Table S3. Comparison of the energy conversion performance of SIM with other ion-selective membranes

Materials	**Diameter**	**Thickness**	**Pore density or porosity**	**$P_{\max}/A$**	**Ref**
PC	15 nm	20 μm	10^5~6×10^8 cm^{-2} 0.05~0.2	0.058[a] ($c_\mathrm{H}/c_\mathrm{L}$ = 1/0.001 M KCl)	S11
Nafion	/	1 mm	/	0.755[a] ($c_\mathrm{H}/c_\mathrm{L}$ = 2/0.001 M KCl)	S12
	3–5 nm	25.4 μm	/	0.00275[a] ($c_\mathrm{H}/c_\mathrm{L}$ = 0.3/0.0001 M KCl)	S13
BNNT	15–40 nm	1 μm	/	4000[c] ($c_\mathrm{H}/c_\mathrm{L}$ = 1/0.001 M KCl)	S14
MoS_2	2–25 nm	0.65 nm	/	10^6[c]	S15
GOM	/	0.5–100 μm	/	0.77[a] ($c_\mathrm{H}/c_\mathrm{L}$ = 0.5/0.01 M NaCl)	S16
RKM	0.68 nm and 1.38 nm	25.1 μm	/	0.18[a] ($c_\mathrm{H}/c_\mathrm{L}$ = 0.1/0.001 M KCl)	S17
MesoC/AAO	MesoC: 7 nm AAO: 80 nm	64.2 μm (MesoC: 4.2 μm AAO: 60 μm)	/	3.46[a] ($c_\mathrm{H}/c_\mathrm{L}$ = 0.5/0.01 M NaCl)	S18
BCP/PET	BCP: 10 nm with 100 nm thick layer and disordered network-like layer; PET: base-500 nm, tip-50 nm	13.5 μm (BCP: 1.5 μm PET: 12 μm)	PET: 10^7 cm^{-2}	0.35[a] ($c_\mathrm{H}/c_\mathrm{L}$ = 0.5/0.01 M NaCl)	S19

Materials		**Diameter**	**Thickness**	**Pore density or porosity**	$\boldsymbol{P_{\mathrm{max}}/A}$	**Ref**
two layers of BCP		top: 17 nm bottom:10 nm	top: 100 nm bottom: 400 nm		2.04^{a} (c_H/c_L = 0.5/0.01 M NaCl)	S20
Silica	nanoslits	height: 4 nm	140 μm	0.25	7.7^{a} (c_H/c_L = 1/0.001 M KCl)	S21
	three-dimensional nanopore networks formed by self-assembled silica nanoparticles	/ (SiO_2: 100 nm)	50 μm	/	2.82^{c} (c_H/c_L = 0.1/0.0001 M KCl)	S22
		15 nm (SiO_2: 100 nm)	200 μm	/	0.008^{a} (c_H/c_L = 0.01/0.0001 M KCl)	S23
	SBA-15	2–3 nm	100 μm	10^{12} cm^{-2}	3.90^{a} (c_H/c_L = 0.3/0.0001 M KCl)	S24
	dense	/ (AAO: 200 nm)	1 μm (AAO: 60 μm)	/ (AAO: 1.2×10^{9} cm^{-2})	0.00098^{a} (c_H/c_L = 0.1/0.01 M NaCl)	S25
	SIM	2–3 nm	90 nm	4×10^{12} cm^{-2} 0.167	212.24^{a}, 0.024^{b} (c_H/c_L = 0.5/0.01 M NaCl) 15.35^{a}, 0.001736^{b} (c_H/c_L = 0.1/0.0001 M KCl)	this work

Abbreviations: PC, polycarbonate; BNNT, boron nitride nanotube; GOM, graphene oxide membrane; RKM, reconstructed kaolinite membranes; MesoC, mesoporous carbon; AAO, macroporous alumina; BCP, block copolymer; PET, polyethylene terephthalate.

[a] P_{max}/A was calculated by dividing the maximum power by the entire cross-sectional area of the ion-selective membrane; In this work*,* A refers the area of the single micropore of SiN, 28.27 μm^2;

[b] A is the dimension of SiN window, 0.25 mm^2.

[c] P_{max}/A was calculated by dividing the maximum power by the pore area of the membrane.

References

S1 Z. Teng, G. Zheng, Y. Dou, W. Li, C.-Y. Mou, X. Zhang, A. M. Asiri and D. Zhao, *Angew. Chem. Int. Ed.*, 2012, **51**, 2173.
S2 X. Lin, Q. Yang, L. Ding and B. Su, *ACS Nano*, 2015, **9**, 11266.
S3 M. Etienne, A. Quach, D. Grosso, L. Nicole, C. Sanchez and A. Walcarius, *Chem. Mater.*, 2007, **19**, 844.
S4 C. Lee, L. Joly, A. Siria, A.-L. Biance, R. Fulcrand and L. Bocquet, *Nano Lett.*, 2012, **12**, 4037.
S5 S. J. Tseng, Y. M. Li, C. Y. Lin and J. P. Hsu, *Electrochim. Acta*, 2016, **219**, 790.
S6 S. Tseng, Y.-M. Li, C.-Y. Lin and J.-P. Hsu, *Nanoscale*, 2016, **8**, 2350.
S7 D.-K. Kim, *J. Mech. Sci. Technol.*, 2011, **25**, 5.
S8 B. D. Kang, H. J. Kim, M. G. Lee and D.-K. Kim, *Energy*, 2015, **86**, 525.
S9 C.-Y. Lin, F. Chen, L.-H. Yeh and J.-P. Hsu, *PCCP*, 2016, **18**, 30160.
S10 L. H. Yeh, C. Hughes, Z. Zeng and S. Qian, *Anal. Chem.*, 2014, **86**, 2681.
S11 K. Kwon, S. J. Lee, L. Li, C. Han and D. Kim, *Int. J. Energy Res.*, 2014, **38**, 530.
S12 T.-C. Tsai, C.-W. Liu and R.-J. Yang, *Micromachines*, 2016, **7**, 205.
S13 H.-K. Chang, E. Choi and J. Park, *Lab Chip*, 2016, **16**, 700.
S14 A. Siria, P. Poncharal, A.-L. Biance, R. Fulcrand, X. Blase, S. T. Purcell and L. Bocquet, *Nature*, 2013, **494**, 455.
S15 J. Feng, M. Graf, K. Liu, D. Ovchinnikov, D. Dumcenco, M. Heiranian, V. Nandigana, N. R. Aluru, A. Kis and A. Radenovic, *Nature*, 2016, **536**, 197.
S16 J. Ji, Q. Kang, Y. Zhou, Y. Feng, X. Chen, J. Yuan, W. Guo, Y. Wei and L. Jiang, *Adv. Funct. Mater.*, 2017, **27**, 1603623.
S17 H. Cheng, Y. Zhou, Y. Feng, W. Geng, Q. Liu, W. Guo and L. Jiang, *Adv. Mater.*, 2017, **29**, 1700177.
S18 J. Gao, W. Guo, D. Feng, H. Wang, D. Zhao and L. Jiang, *J. Am. Chem. Soc.*, 2014, **136**, 12265.
S19 Z. Zhang, X. Y. Kong, K. Xiao, Q. Liu, G. H. Xie, P. Li, J. Ma, Y. Tian, L. P. Wen and L. Jiang, *J. Am. Chem. Soc.*, 2015, **137**, 14765.
S20 Z. Zhang, X. Sui, P. Li, G. Xie, X.-Y. Kong, K. Xiao, L. Gao, L. Wen and L. Jiang, *J. Am. Chem. Soc.*, 2017, **139**, 8905.
S21 D.-K. Kim, C. Duan, Y.-F. Chen and A. Majumdar, *Microfluid. Nanofluid.*, 2010, **9**, 1215.
S22 W. Ouyang, W. Wang, H. Zhang, W. Wu and Z. Li, *Nanotechnology*, 2013, **24**, 345401.
S23 E. Choi, K. Kwon, D. Kim and J. Park, *Lab Chip*, 2015, **15**, 168.
S24 J. Hwang, S. Kataoka, A. Endo and H. Daiguji, *Lab Chip*, 2016, **16**, 3824.
S25 S. Lee, H. Kim and D.-K. Kim, *Energies*, 2016, **9**, 49.